

RSC Applied Interfaces

Accepted Manuscript

This article can be cited before page numbers have been issued, to do this please use: F. G. Svensson, E. Djurberg, Y. Yan, S. Kim, J. Henych, J. Tolasz, F. Dappozze, S. Parola, C. Guillard, B. I. Stefanov and L. Ö. Österlund, *RSC Appl. Interfaces*, 2026, DOI: 10.1039/D5LF00398A.



This is an Accepted Manuscript, which has been through the Royal Society of Chemistry peer review process and has been accepted for publication.

Accepted Manuscripts are published online shortly after acceptance, before technical editing, formatting and proof reading. Using this free service, authors can make their results available to the community, in citable form, before we publish the edited article. We will replace this Accepted Manuscript with the edited and formatted Advance Article as soon as it is available.

You can find more information about Accepted Manuscripts in the [Information for Authors](#).

Please note that technical editing may introduce minor changes to the text and/or graphics, which may alter content. The journal's standard [Terms & Conditions](#) and the [Ethical guidelines](#) still apply. In no event shall the Royal Society of Chemistry be held responsible for any errors or omissions in this Accepted Manuscript or any consequences arising from the use of any information it contains.

ARTICLE

Photo-deposition of Cu₂O on Pre-Annealed ZnO Nanorods Yields pn-Type Heterostructures with Enhanced Photocatalytic ActivityFredric G. Svensson,^{† a} Erik Djurberg,^a Yige Yan,^{b,c} Seohan Kim,^d Jiri Henych,^{e,f} Jakub Tolasz,^e Frederic Dappozze,^c Stephane Parola,^b Chantal Guillard,^c Bozhidar I. Stefanov,^g and Lars Österlund^{*h}Received 00th January 20xx,
Accepted 00th January 20xx

DOI: 10.1039/x0xx00000x

Copper–zinc oxide pn-type heterostructures are promising visible-light-active photocatalysts because their intrinsic bandgaps and band alignment facilitates efficient charge separation. However, achieving controlled deposition of copper oxide nanoparticles on ZnO nanorods remains challenging, particularly in forming well-defined interfaces. Here, we report a UV-assisted photo-deposition method using [Cu(EDTA)]²⁻ complexes to predominantly form Cu₂O nanoparticles on sea-urchin-like ZnO nanorods that either were used as-prepared or subjected to systematic post-heating treatments. The structural, chemical, and electronic properties of the resulting pn-type heterostructures were characterized by X-ray diffraction, electron microscopy, photoelectron and photoluminescence spectroscopy, while phenol photodegradation products were quantified by HPLC. In contrast to as-prepared ZnO nanorods, annealing treatment prior to Cu₂O deposition produces well-developed Cu₂O–ZnO interfaces, yielding pn-type heterostructures with enhanced photocatalytic degradation of phenol under UVA illumination. Our results indicate improved interfacial charge transfer, attributed to reduced lattice defects and removal of surface contaminants through annealing. These findings demonstrate that substrate surface preparation combined with atom-by-atom photo-deposition of chelated copper complexes provides a straightforward route for optimizing heterostructure catalysts with improved interfacial properties and enhanced photocatalytic activity.

1. Introduction

Heterogenous photocatalysis has been extensively investigated for the remediation of water contaminated with pollutants over the last decades.^{1, 2} Despite extensive search for new, efficient photocatalysts, in particular visible-light active photocatalysts, TiO₂ and ZnO remains the dominant metal oxides for environmental photocatalysis due to their high activity, availability and ease of preparation.³ TiO₂ and ZnO are however wide bandgap metal oxide semiconductors and rely on UV illumination ($\lambda < 390$ nm) for electron-hole pair generation and subsequent radical formation (e.g. O₂^{•-}, OH[•]), which makes their application under solar light inefficient as only some 5 %

of the solar radiation are energy-rich enough for bandgap illumination.⁴

Heterostructure catalysts can help overcome this limitation by combining appropriate constituent materials, but they introduce challenges in achieving efficient charge separation of excited electron-hole pairs and establishing good electronic contact across material interfaces. In assemblies of p-type and n-type nanoparticles, the formation of a functional pn-type heterostructures differs fundamentally from that in epitaxially grown films, where smooth, parabolic band bending across a well-defined depletion region is established, enabling efficient charge separation via a strong built-in electric field. In contrast, a pn-type nanoparticle junction is typically formed by the physical contact of two pre-synthesized nanocrystals. The interface is a disordered, zero-dimensional point contact between curved surfaces with misaligned crystal lattices. This structural imperfection, combined with the inherently high surface-to-volume ratio of nanoparticles, introduces a high density of mid-gap defect states. These states act as electron traps and pin the Fermi level at the interface. Consequently, band bending becomes localized, irregular, and inefficient with incompletely developed depletion regions, typically just the surface layers. Charge transfer across this junction often occurs via trap-assisted tunnelling or hopping leading to higher recombination losses. In photocatalytic processes, interfacial charge transfer—specifically, the transfer of excited electrons and holes from the particle surface to adsorbed oxygen and water/hydroxyl groups, respectively—is often the rate-limiting step for overall efficiency.⁵ It is therefore desirable to develop

^a Department of Materials Science and Engineering, The Ångström Laboratory, Uppsala University, Uppsala Box 35, 751 03, Sweden.

^b Laboratoire de Chimie, UMR 5182, ENS de Lyon, 69364 Lyon Cedex 07, France.

^c Institut de recherches sur la catalyse et l'environnement de Lyon (IRCELYON), CNRS - Université Lyon 1, UMR5256, 69626 Villeurbanne Cedex, France.

^d Yeongnam Regional Center, Korea Basic Science Institute, Rep Korea, 46742.

^e Institute of Inorganic Chemistry of the Czech Academy of Sciences, Materials Chemistry Department, 250 68 Husinec-Řež, Czechia.

^f Faculty of Environment, Jan Evangelista Purkyně University in Ústí nad Labem, Pasteurova 3632/15, 400 96 Ústí nad Labem, Czechia.

^g Department of Chemistry, Faculty of Electronic Engineering and Technologies, Technical University of Sofia, 8 Kliment Ohridski Blvd, 1756 Sofia, Bulgaria.

^h Department of Chemistry, Umeå University, 901 87 Umeå, Sweden.

E-mail: lars.osterlund@umu.se

[†] Present address: Department of Molecular Sciences, Swedish University of Agricultural Sciences, Box 7015, Uppsala 75007, Sweden.

Supplementary Information available: [details of any supplementary information available should be included here]. See DOI: 10.1039/x0xx00000x



methods to improve the interface structure in pn-heterostructure photocatalysts to allow built-in fields to develop and spatially separate the photo-excited electrons and holes.⁶

One of the most extensively studied pn-heterostructure systems for photocatalytic applications is Cu(I,II)O@ZnO,⁷⁻⁹ where CuO (and Cu₂O) acts as the p-type semiconductor and ZnO as the n-type semiconductor. The Cu 3d–O 2p valence states of Cu₂O hybridize with the O 2p valence states of ZnO, because O 2p orbitals bridge both cations, forming separate bands that align and interact at the interface.¹⁰ The conduction band edge of ZnO is lower than that of CuO, resulting in the flow of photo-excited electrons from CuO to ZnO, where O^{2-•} radicals are formed.¹¹ CuO@ZnO composites are reported to exhibit improved light absorption over the entire visible range compared to pure ZnO.¹¹⁻¹³ Holes in CuO react with water to form OH[•] radicals.¹⁴ However, preparing Cu(I,II)O/ZnO pn-heterostructures with well-developed interfaces remains challenging, as interfacial lattice imperfections and surface impurities introduce energy barriers that hinder charge transfer. In the case of ZnO, this is further challenged by the well-known deep bandgap states in ZnO nanoparticles.^{15, 16} Recently, elaborate metal-organic framework homojunction structures have been reported,¹⁷ highlighting the importance of careful design to achieve well-defined junctions.

Several methods to prepare CuO@ZnO pn-heterostructures have been reported, including solid-state reactions between copper and zinc salts,¹⁸ co-precipitation,¹⁹ solution combustion,²⁰ and sol-gel methods.^{8, 21} The CuO@ZnO composites have been reported to exhibit 2-4 times better decomposition of pollutants during photocatalysis compared to the individual components.^{7, 13} There is also significant interest in well-defined CuO@ZnO nanocomposites due to their application in methanol synthesis.^{22, 23}

Recently, hydrothermally prepared, vertical ZnO rods were used as support to deposit Cu₂O by advanced gas deposition method.²⁴ The resulting composite exhibited improved charge transfer, attributed to the high-quality interface achieved by vacuum deposition. As an alternative, purely wet-chemical approach for in situ surface functionalization of photocatalysts with secondary phases for heterostructure formation, photo-deposition utilizes photogenerated charge carriers to directly reduce precursor metal ions to their metallic form or to deposit the corresponding metal oxides through reactions with photogenerated reactive oxygen species. Photo-deposition has been most widely applied to TiO₂ photocatalysts and is a well-understood process.^{25, 26}

Simple Cu(II) salts, such as aqueous cupric nitrate, are often directly used as Cu_xO precursors in photo-deposition electrolytes.^{27, 28} However, this approach limits the ability to tune reaction parameters—such as pH—which can influence the stoichiometry of the photo-deposited products, as illustrated by copper's Pourbaix diagram.^{29, 30} As a result, a mixture of Cu⁰, Cu₂O, and CuO phases is typically obtained. To improve control over the photo-deposition process, chelated Cu(II) species such as [Cu(EDTA)]²⁻—commonly used in electroless plating—can be employed. These complexes are

stable across a wide pH range. For instance, Venev et al.³¹ reported on the wet-chemical photo-deposition of metallic copper on TiO₂, using [Cu(EDTA)]²⁻ complex at pH 13, with formaldehyde as a reducing agent, to form conductive patterns on the TiO₂ surface. Follow-up studies using the same system demonstrated that at lower pH, a mixed Cu₂O/CuO oxide phase (in a 3:1 ratio) is deposited on the TiO₂ surface.³² However, the photocatalytic performance of the functionalized TiO₂ catalysts was not addressed in either of these studies.

Although numerous studies have reported Cu_xO photo-deposition on TiO₂, this method is less frequently explored for ZnO—and seldom using chelated copper precursors.^{30, 33} Such an approach could be advantageous, as it allows for functionalization at near-neutral pH, thereby preventing ZnO dissolution caused by the acidic cupric nitrate solutions commonly used.

In the present study we apply post-heating of ZnO nanoparticles to remove mid-gap states to overcome Fermi level pinning. The photo-deposition of Cu atoms facilitates growth of Cu₂O bottom-up on the ZnO surface facilitating more developed oxide interface. We provide evidence that the resulting cleaner electronic interface enhances the driving force for charge separation, promoting direct band-to-band electron transfer from Cu₂O to ZnO, and reduces trap-mediated recombination.

2. Materials and methods

2.1 Materials

“Sea urchin”-like ZnO nanorods were prepared by a low-temperature method. Zinc acetate dihydrate (reagent grade, Sigma-Aldrich) (1.5 g) was dissolved in deionized (DI) water to a concentration of 0.27 M (25 mL). This was added to a 2.73 M (2.73 g) sodium hydroxide solution (25 mL), to give a reaction mixture with a total volume of 50 mL and final concentrations of Zn²⁺ and OH⁻ of 0.135 M and 1.37 M, respectively. The Zn²⁺:OH⁻ molar ratio was 1:10. The solution was heated at 50°C in a water for 90 min. After about 10 min, the solution turned slightly opaque, and after 90 min a massive precipitation of sea urchin-like ZnO had occurred. The precipitate was washed with DI water and centrifuged until the supernatant had reached neutral pH, to obtain the ZnO stock denoted as “as-prepared”. The “post-heated” ZnO was prepared from it by annealing in air the as-prepared ZnO for 30 min at 500°C in a furnace with 20 min temperature ramp.

Copper acetate monohydrate (98 %, Aldrich) was dissolved in 25 mL DI H₂O and 1 equivalent of disodium EDTA (99 %, Merck) dissolved in 25 mL DI H₂O was added. The final Cu²⁺ concentration was 0.1 M. The color changed from light blue to dark blue upon mixing, confirming complexation. The pH of this solution was about 3.8. The pH was then adjusted to 5.1 by dropwise addition of 1 M NaOH (99 %, Merck). The [Cu(EDTA)]²⁻ solution was stored in darkness at room temperature.

The photo-deposition followed a method adapted from ideas presented by Venev et al.³¹; 100 mg ZnO (post-heated or



as-prepared) was placed in an 18 mL ceramic crucible together with an 8 mm Teflon-coated magnetic stirrer. Then, 1.5 mL of the $[\text{Cu}(\text{EDTA})]^{2-}$ solution (Zn/Cu ratio of $\sim 8:1$) was added and stirred at 300 rpm. A UV source was placed 2.5 cm over the solution surface, and the reaction mixture was illuminated with a 365 nm LED light source (19 mW/cm², FWHM = 12 nm; Prizmatix Ltd., Holon, Israel) for 1 hour under stirring by a Teflon line magnet (400 rpm). The white powder turned brown-orange after completed photo-deposition (see Supplementary Fig. S1). The resulting Cu-Zn oxide composite was separated by centrifugation and washed with DI H₂O several times before air-dried at ambient conditions. The product powder remained brown-orange after washing with no apparent color shift over time. Cu₂O (99 %, Aldrich) was used for preparation of physical Cu₂O/ZnO mixtures as reference samples. These were prepared by physically mixing the appropriate amounts of dry ZnO (as-prepared) and Cu₂O powders for a total weight of 100 mg, where 5 w% or 15 w% constitute Cu₂O.

2.2 X-ray diffraction

The as-prepared and post-heated ZnO was characterized by powder X-ray diffraction (PXRD). A Siemens D5000 powder X-ray diffractometer with Cu K_{α,II} radiation ($\lambda = 1.5418 \text{ \AA}$) and Bragg-Brentano geometry was used. The step size was set to 0.02° and divergence- and anti-scattering slit widths of 1° were used. The Cu-Zn oxide composites were deposited on glass slides and analyzed by grazing incidence XRD (GIXRD) (Siemens D5000 diffractometer with Cu K_{α,II} radiation ($\lambda = 1.5418 \text{ \AA}$) with 0.03° step size and step time of 1 second). From the diffractograms, the average coherent crystallite sizes were estimated by the Scherrer equation, $D = K\lambda / (B_c \cos\theta)$, where D is the mean crystallite size, K is a shape factor (here 0.94), B_c is full width at half maximum (FWHM) corrected for instrumental broadening (NIST 1976 Al₂O₃ standard) and θ is the Bragg angle in radians. The average crystallite sizes for ZnO were from the FWHM of the (1 0 1) diffraction plane.

2.3 Electron microscopy

For morphological characterization and determination of elemental composition of the materials, a Zeiss LEO 1550 scanning electron microscope (SEM) equipped with a field emission gun (operated between 3 keV and 8 keV) and an Oxford Aztec energy dispersive X-ray spectroscopy (EDS) system was employed. All powder samples were dispersed on carbon tape for analysis.

Lattice spacing measured from selected area electron diffraction (SAED) were obtained using a field-emission transmission electron microscopy (FE-TEM, JEOL, JEM-2100F). Phase identification was conducted with selected ZnO references from the PDF-5+ database suggested for ICDD 04-06-1673. For STEM-EDS analysis, a Thermo Fisher Scientific FEI Talos F200X scanning/transmission electron microscope equipped with Super-X EDX detector system was used. The samples were deposited on holey carbon grid from water suspension and air-dried before their inspection.

2.4 X-ray photoelectron spectroscopy

The oxidation states of copper were analyzed by X-ray photoelectron spectroscopy (XPS) employing a Quantera II Scanning XPS Microprobe (Physical Electronics) equipped with an Al K_α source. A low-energy flood-gun operating at 1.0 V and 20.0 μA beam current was used for charge compensation. For the survey spectra, a pass energy of 224 eV and a resolution of 0.8 eV was used, and for high-resolution spectra a pass energy of 55 eV and 0.1 eV resolution were used. The spectra were calibrated against the 284.8 eV peak due to adventitious carbon. To investigate possible oxidation of Cu during photocatalysis, high resolution XPS of Cu and O were recorded before and after photocatalytic degradation of phenol.

2.5 Surface area measurements

A Micromeritics ASAP 2020 instrument was used to determine the surface areas of the two different Cu₂O@ZnO pn-type heterostructure catalysts by means of BET analysis. The samples were pre-dried in a furnace at 120°C for 2 h, then stored in sealed plastic vessels in a desiccator before degassing under vacuum at 120°C for 2 h prior to analysis.

2.6 Photoluminescence spectroscopy

Photoluminescence spectroscopy (PL) was used to measure the near bandgap emission and deep level emission of the investigated samples. An Edinburgh Instrument FLS1000 equipped with a halogen lamp employing 360 nm emission wavelength was used to collect emission spectra at room temperature on drop casted powder samples dispersed in ethanol on quartz substrates. Triplicate scan spectra were acquired with 1 nm step size and 0.1 s dwell time in the range 360 nm to 825 nm. The presented deep level emission bands were normalized against the integrated near-band emission (NBE) ZnO line for each spectrum occurring at 368 nm (3.37 eV), which we assume is not affected by Cu photo-deposition.

2.7 Photocatalytic degradation of phenol

Photocatalytic degradation tests were conducted by using a 100 ml Pyrex photo-reactor in air atmosphere. Phenol (99%, Sigma-Aldrich) was employed as model-pollutant. For all the experiments, the concentration of the photocatalyst was set to 1 g·L⁻¹. In detail, 100 mg of catalyst were added to 100 mL of a solution of the pollutant (60 ppm) with top motorized stirring for 60 min in the dark to reach equilibrium. A pre-heated UV-A PL-L 18W (Philips) was positioned under the reactor. The irradiation at 365 nm measured on the inner bottom side of the reactor was 4.8 mW/cm². 0.8 mL of the solution was sampled and filtrated on an MILLEX HVLP 0.45 μm hydrophilic filter (Millipore, Burlington, MA, USA) for the HPLC analyses.

HPLC analyses for phenol was performed using a Shimadzu system (Shimadzu, Japan) equipped with a photodiode array detector and a 150 mm × 4.6 mm × 2.7 μm -Ascentis Express 90



A° AQ-C18 column (Supelco Merck). The mobile phase was a 95 %v / 5%v acidified Water (with 0.1%w/w HCOOH) / Methanol mixed solution. The flow rate was set at 1.0 mL min⁻¹. The column working temperature was set at 40°C.

3. Results and discussion

3.1 Structure and morphology

Fig. 1 shows the indexed X-ray diffraction (XRD) diffractograms of the Cu-Zn oxide samples using grazing incidence XRD (GIXRD) was used. Despite a noticeable change from white to pale orange-brown color on the Cu-deposited Zn oxide samples, crystalline phases other than ZnO could not be detected by Bragg-Brentano geometry. The average crystallite sizes for as-prepared and post-heated ZnO were 41.8 nm and 55.9 nm, respectively, as determined by Scherrer analysis. From GIXRD several copper oxide related phases could be detected, mainly Cu₂O (cubic, space group Pn-3m), and minority CuO (monoclinic, space group C2/c) and metallic copper (cubic, space group Fm-3m) diffraction peaks, which are in good agreement with XPS results below. We therefore denote the heterostructures “Cu₂O@ZnO” as the majority copper oxide phase is Cu₂O. Crystallite size was determined by Scherrer analysis of the FWHM of XRD reflections after correcting for instrumental broadening. The crystallite sizes for Cu₂O were estimated to 16.6 nm and 23.7 nm for Cu₂O@ZnO (as-prepared) and Cu₂O@ZnO (post-heated), respectively, using Scherrer calculation. The average crystallite sizes for metallic Cu were calculated to 15.0 nm and 20.1 nm for Cu₂O@ZnO (as-prepared) and Cu₂O@ZnO (post-heated), respectively, showing consistently that the crystallites grow larger on the post-heated material. We interpret this to larger mobility of the Cu species on the post-heated ZnO due to reduced number of nucleation sites on the surface. A digital photograph of the Cu₂O@ZnO powder is shown in Supplementary Fig. S2. Moderate stirring

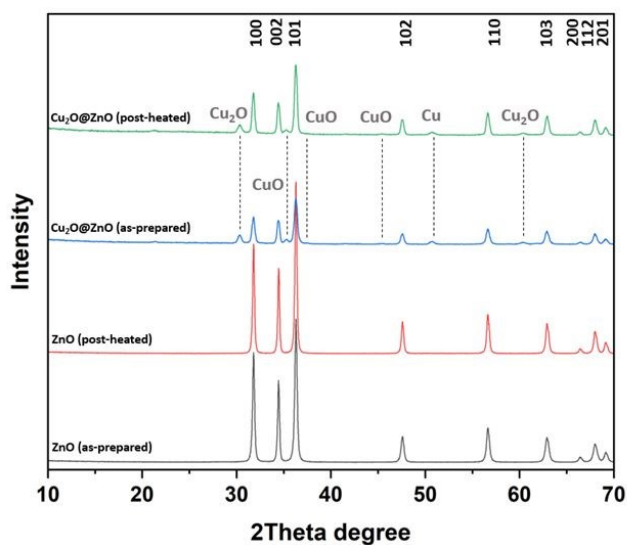


Fig.1 Indexed diffraction patterns for the four photocatalysts labelled at each diffractogram. The ZnO patterns corresponds to the reference pattern for the wurtzite phase (ICCD #04-006-1673). The copper-related patterns were indexed as metallic Cu (ICCD #04-001-3178), Cu₂O (ICCD #04-006-6514), and CuO (ICCD #00-048-1548).

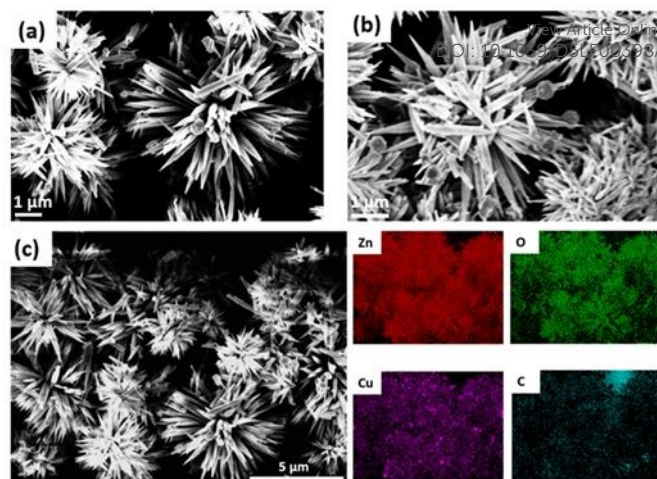


Fig. 2 (a, b) Representative SEM micrographs of Cu₂O@ZnO deposited on post-heated ZnO. (c) a cluster Cu₂O@ZnO deposited on post-heated ZnO with elemental mapping, confirming the presence of zinc, oxygen, and copper. About 50 copper spheres can be seen in Fig. 2c.

(300 rpm) was required as only the solution-exposed part of the ZnO would be deposited otherwise. The specific surface areas for Cu₂O@ZnO (as-prepared) and Cu₂O@ZnO (post-heated) were determined to 11.7±0.2 m²/g and 7.8±0.4 m²/g, respectively.

Fig. 2 shows SEM images of Cu deposited on post-heated ZnO, exhibiting sea urchin-like structures with diameters between 2 μm to 5 μm. The sea urchin-like structures were intact after the Cu photo-deposition synthesis step. No evident observable changes in morphology were seen for the as-prepared ZnO (Supplementary Fig. S3). As evident from the elemental maps in Fig. 2, copper appears evenly distributed over the ZnO samples, which is also confirmed by TEM analysis showing homogenous deposition of nano copper containing particles over the ZnO rods (**Fig. 3**). Detailed analysis of the SEM images show that the Cu₂O@ZnO samples consist of small particles decorating the ZnO rods, but also larger, about 100 nm, aggregates of smaller copper oxide nanoparticles spheres that according to the elemental analysis mainly consist of copper in different oxidation states, as elaborated in the XPS section below (Fig. 3). TEM shows that those particles mainly exist at the tips of the ZnO rods (Fig. 3b), suggesting that these are sites for nucleation of excess Cu. High-resolution STEM-EDS confirms that those spheres consist of Cu and Cu₂O (**Fig. 4**).

A tentative explanation for this may be that the alternating positive and negative planes within the wurtzite structure causes an internal electric field which promotes the separation of the photo-excited electron-hole pair. Electrons migrate towards the positive (001) plane where reduction reactions may occur.³⁴ It might then be possible that an increased concentration of electrons at the ZnO tips facilitates reduction and nucleation of metallic Cu and Cu₂O, causing the formation of observed spheres, thus providing an explanation for the weak metallic Cu peaks in XRD seen in Fig. 1. The formation of Au nanoparticle spheres on the tips of CdSe and CdSe/CdS nanorods under illumination has been reported.³⁵ It is known that direct electrical pathways provided by ZnO nanowires



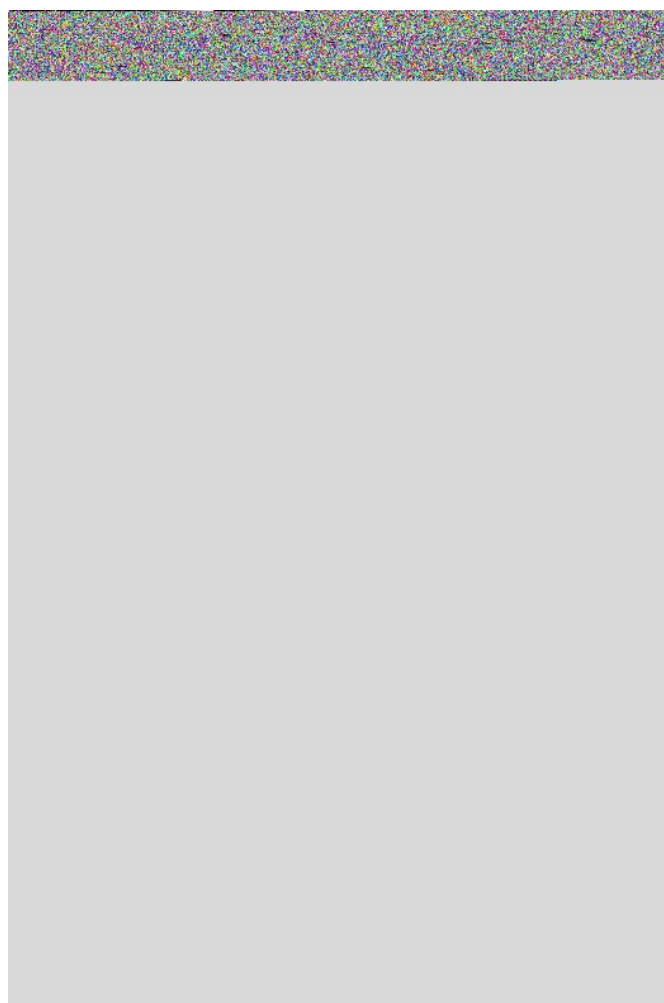


Fig. 3 TEM micrographs of (a) ZnO post-heated, and (b, c) Cu₂O@ZnO (post-heated). (d-f) EDS analyses of Cu₂O@ZnO, confirming the presence of Zn, O, and Cu, respectively.

facilitate rapid collection of carriers that are formed throughout connect wires.³⁶ The sea urchin-like structures seen in Fig. 2 may thus expose a higher effective surface for photo-induced redox surface reactions than the directly illuminated fraction of the sample.

3.2 Chemical composition

Fig. 5 shows high-resolution spectra of Cu₂O@ZnO samples before and after photocatalytic degradation of phenol. Survey spectra are presented in Supplementary **Fig. S4a, b**, while binding energies and elemental composition are shown in **Table S1**. Here we focus the analysis of the Cu-complexes deposited on post-heated ZnO. The electron binding energies of metallic copper and Cu¹⁺ (as in Cu₂O) are overlapping and not easily separated. In contrast, the Cu¹⁺ and Cu²⁺ (in Cu₂O and CuO) positions are separated by about 1.3 eV.³⁷ Deconvoluting the high-resolution spectrum for samples before photocatalysis for Cu 2p_{3/2} (**Fig. 5a**) results in two major components centred at 931.6 eV and 933.6 eV which corresponds to Cu⁺ and Cu²⁺, respectively. Quantifying their relative intensities from the integrated area shows gives an approximate Cu⁺ to Cu²⁺ ratio of about 2:1. It is however expected that Cu-OH contribute above

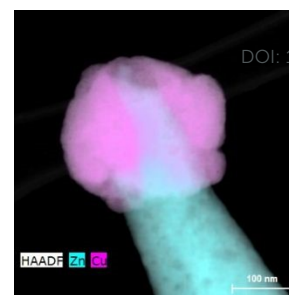


Fig. 4 High-resolution STEM-EDS micrograph of the tip of a ZnO rod (blue) with copper and copper oxide grown on the tip (purple).

about 934 eV, which also can be discerned in Fig. 5, and contribute to the Cu²⁺ band, and thus lower the Cu²⁺ contribution. The distinction between Cu²⁺-(OH)₂ and Cu²⁺-O is however difficult in XPS and was not attempted here due to large S/N in the Cu 2p spectra. For the samples analysed before the photocatalysis experiments the two characteristic Cu²⁺ satellites can be observed between 940 eV and 945 eV (**Fig. 5a**). These satellites are found for Cu²⁺ (as in CuO) and confirm the presence of a CuO phase. XPS is however expected to show larger amounts of CuO than inferred from the XRD data since it is a surface-sensitive technique due to oxidation of the outermost Cu deposition to CuO in oxidizing environment, which is not representative for the deeper Cu-Zn oxide interface. After photocatalysis (**Fig. 5c**) the Cu²⁺ satellite peaks decreased while the integrated areas Cu²⁺: Cu⁺ remained approximately the same, again suggesting that Cu-OH contributes to the deconvoluted Cu²⁺ band. The peak for the

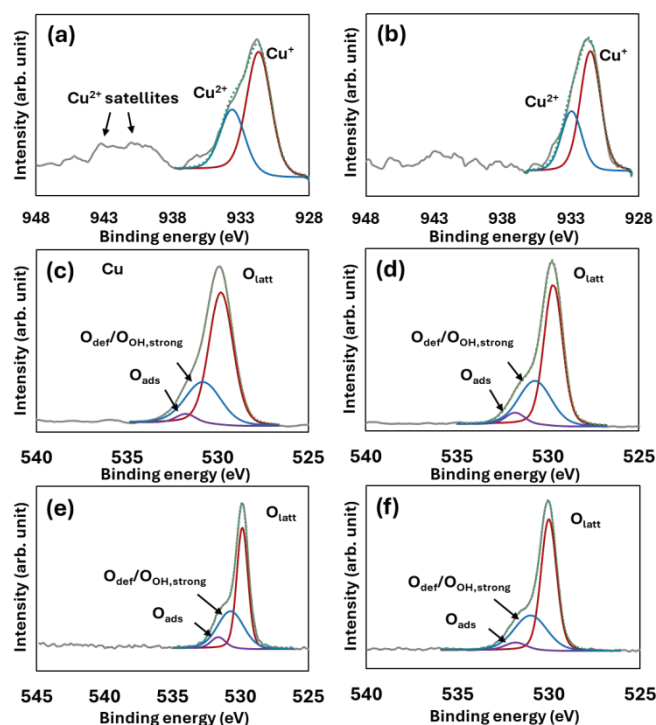


Fig. 5 High resolution XPS spectra of Cu₂O@ZnO (post-heated) and ZnO (as-prepared and post-heated). Cu 2p_{3/2} of Cu₂O@ZnO before (a) and after (b) photocatalysis. O 1s spectra of Cu₂O@ZnO before (c) and after (d) photocatalysis. O 1s spectra of ZnO (as-prepared) (e) and ZnO (post-heated at 500°C for 30 min) (f). The deconvoluted contributions of Cu⁺ and Cu²⁺ are indicated. The O 1s spectra due to Cu²⁺ – O_{ads}/O_{def/OH,strong} and Zn – O_{ads}/O_{def/OH,strong} overlap and are represented by one band each.



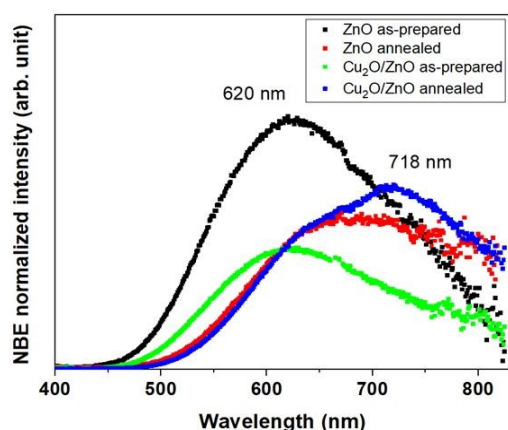


Fig. 6 Near-band edge (NBE) normalized photoluminescence spectra of as-prepared annealed ZnO nanorods, and corresponding spectra of $\text{Cu}_2\text{O}/\text{ZnO}$, showing deep level emission states.

$2p_{3/2}$ peak at 931.5 eV did not change much. A previous study on the photodecomposition of $[\text{Cu}(\text{EDTA})]^{2-}$ over TiO_2 also found metallic Cu and Cu_2O depositions over the TiO_2 .³⁸

To get further insight into the chemistry of the mixed oxide, the O 1s peak was analyzed. Based on the high copper coverage from SEM-EDS and TEM-EDS analysis, along with the short penetration depth of XPS, it is reasonable to assume that both Cu and Zn oxides contribute to the O 1s signal. The O 1s position of Cu^+ and Cu^{2+} differ slightly and can provide further information about the different oxide phases. It has been reported that the component at ~ 530 eV represents O in Cu_2O , and the higher binding energy (~ 530.6 eV) is O in CuO .⁴⁰ In addition, surface OH due to both Zn and Cu is expected to contribute to the O 1s spectra, where the component at ~ 531.8 eV represents Zn-OH/Cu-OH.⁴¹ Furthermore, the as-prepared ZnO was previously determined to have more surface hydroxyls compared to post-heated ZnO,³⁹ and it is reasonable that surface OH are replenished upon photocatalysis. Fig. 5c and d show O 1s spectra before and after photocatalysis, respectively. The O 1s shift was deconvoluted into three components due to lattice oxygen (O^{2-} in metal oxide), defect-associated oxygen and/or strongly bound surface hydroxyls, and adsorbed oxygen species (e.g., weakly bound OH, H_2O , carbonates, organics), with binding energies at 529.8 eV, 530.8 eV, and 531.8 eV, respectively (Fig. 5c). The O 1s binding energies remained approximately the same after photocatalysis. Before photocatalysis, the Cu^+ , Cu^{2+} , and Zn-OH/Cu-OH distribution is ≈ 66 at.%, ≈ 30 %, and ≈ 3 at.%, respectively, and after photocatalysis ≈ 62 at. %, ≈ 33 at.%, and ≈ 5 at.%, respectively, showing slight surface oxidation of the Cu oxide during photocatalysis. In comparison, pure ZnO (as-prepared) and ZnO (post-heated at 500°C for 30 min) from our previous work³⁹ contained 6 at.% and 5 at.% Zn-OH, respectively (Figure 5e, f) indicating that surface hydroxyls and defect-associated oxygen are depleted during photo-deposition of Cu, and gradually formed during photocatalysis. As discussed below, surface OH contributes to the initial phenol photodegradation and thus affects the comparison between ZnO and $\text{Cu}_2\text{O}/\text{ZnO}$ samples. Finally, it should be noted that due to the very small shifts of $\text{Cu}^{2+} - \text{O}_{\text{ads}}/\text{O}_{\text{def}}/\text{OH-strong}$ and $\text{Zn} - \text{O}_{\text{ads}}/\text{O}_{\text{def}}/\text{OH-strong}$, deconvoluting

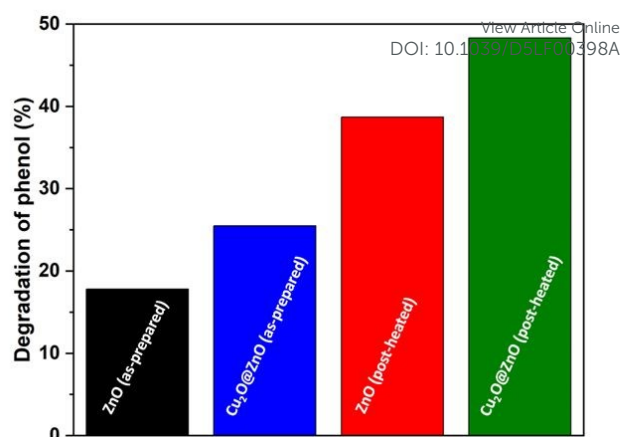


Fig. 7 Percent degradation of phenol by the four different photocatalysts after 3 hours of UV-A illumination.

their separate contributions is very difficult and are therefore here presented as the combined contribution.

3.3 Electronic structure and interfacial charge transfer

It is evident that post-heating the samples for 30 min at 500°C almost completely removes the deepest emission band at about 620 nm regardless of Cu_2O is photo-deposited on the ZnO rods, or not. Photo-deposition of as-prepared ZnO with Cu_2O nanoparticles ($\text{Cu}_2\text{O}/\text{ZnO}$ -as-prepared) quenches the 620 nm emission band, although not eliminating it. A new emission line at about 718 nm appears on post-heated ZnO with deposited Cu_2O nanoparticles ($\text{Cu}_2\text{O}/\text{ZnO}$ -post-heated) which is not clearly resolved for the $\text{Cu}_2\text{O}/\text{ZnO}$ -as-prepared sample. Emission bands due to excitons are not observed at room temperature⁴², and there are no observable bands in the 430 nm to 470 nm region, which have been attributed to surface states, adsorbates, or small metallic Cu clusters.⁴³ No emission due to Cu_2O was observed in any of the samples (except to occur around 600 nm), indicating efficient quenching of interband decay with Cu_2O . The latter is augmented by the indirect-like optical properties of Cu_2O due to the dipole-forbidden nature of the optical transition at the Γ point. Comparing with previously reported data on the band edge and Fermi level position for $\text{Cu}_2\text{O}/\text{ZnO}$ heterostructures,^{24, 44} we therefore attribute the 718 nm emission due to interfacial radiative recombination across the $\text{Cu}_2\text{O}/\text{ZnO}$ heterostructure. Electron from ZnO conduction band recombines with hole in Cu_2O valence band, giving a lower-energy emission that is not present in pure ZnO. The 718 nm emission (about 1.73 eV) is below Cu_2O bandgap, consistent with type-II band alignment interfacial recombination.

We note that quenching of the deep level emission band after post-heating ZnO nanorods correlates with the disappearance of OH and hydride species bonded to lattice defects (O vacancies and Zn interstitials) as the ZnO becomes more crystalline and defects are healed upon annealing.³⁹ The disappearance of those defects has been shown to decrease the initial rate of photocatalytic degradation of phenol due to loss of OH radicals generated from these sites.³⁹ As we show in the



next section, $\text{Cu}_2\text{O}@ZnO$ can therefore not per se be expected to promote phenol photo-degradation if those sites are blocked by Cu_2O nanoparticles. Hence, a trade-off is apparent. While post-heating ZnO yields $\text{Cu}_2\text{O}@ZnO$ with improved electronic coupling across the $\text{Cu}_2\text{O}/ZnO$ interfaces, Cu_2O deposition and post-heating blocks and reduces photocatalytic active OH and hydride species. In the next section, we quantify these counteracting effects.

3.4 Photocatalytic degradation of phenol

To qualitatively validate the hypothesis of improved electron-hole pair separation due to charge transfer across pn-junctions, the photocatalytic degradation of an aqueous phenol solution (60 ppm) under UVA illumination was studied over a period of three hours. Phenol was chosen as model organic compound since the decomposition chemistry and intermediate steps are well-known and can be accurately measured. The decomposition was followed by HPLC-PDA. It was found that the post-heated ZnO and $\text{Cu}_2\text{O}@ZnO$ degraded phenol much faster compared to the as-prepared ZnO and $\text{Cu}_2\text{O}@ZnO$ samples. After 3 hours of UV illumination, as-prepared ZnO, as-prepared $\text{Cu}_2\text{O}@ZnO$, post-heated ZnO, and post-heated $\text{Cu}_2\text{O}@ZnO$ showed 17.8 %, 25.5 %, 38.7 %, and 48.3 % degradation of the initial phenol, respectively (Fig. 7). The concentration of phenol as a function of illumination time and corresponding pseudo-first order plots are shown in Fig. 8. The corresponding degradation rate constants are presented in Table 1. It is seen that the post-heated ZnO and $\text{Cu}_2\text{O}@ZnO$ catalysts yield markedly higher rates compared to those based on as-prepared ZnO. Phenol without any catalyst did not show any degradation under UV-illumination. The effect of only Cu_2O and physical mixtures of Cu_2O with ZnO (as-prepared) at two different concentrations (5 weight% and 15 weight% Cu_2O) were also investigated (Supplementary Fig. S5). Cu_2O had very low photocatalytic activity, with 95 % of phenol remaining after 180 min of UV illumination. The physical mixture $\text{Cu}_2\text{O}/ZnO$ (as-prepared) with 5 wt% and 15wt% Cu_2O showed 17.4 % and 21.6% phenol degradation over 180 min. Thus, simple physical mixing of Cu_2O and ZnO gives marginally better decomposition

than as-prepared ZnO, but less than $\text{Cu}_2\text{O}@ZnO$ (as-prepared). It is seen in Supplementary Figure S5 that the physical addition of 5 wt% or 15wt% Cu_2O differs little in degradation. Hence, we conclude that attachment of Cu_2O on ZnO by photo-deposition enhances the photocatalytic activity. It is evident by comparing Fig. 8 and Fig. S5 that the post-heated $\text{Cu}_2\text{O}/ZnO$ heterostructure gives much higher photodegradation activity than what can be explained by the constituent materials, but that the as-prepared photo-deposited $\text{Cu}_2\text{O}/ZnO$ only has slightly higher activity (25.5 %). It is further seen that an increased Cu_2O loading in the physical ZnO and Cu_2O mixtures increases the phenol degradation activity, but even with a Cu_2O loading much larger than what we estimate on the photo-deposited $\text{Cu}_2\text{O}/ZnO$ samples (15 wt% Cu_2O), the phenol degradation is still lower than what is observed on the “as-prepared” photo-deposited $\text{Cu}_2\text{O}/ZnO$. These observations indicate that the pn-heterostructures deposited on defect-rich and contaminated ZnO surfaces (from synthesis residues and non-perfect crystallization) suffer from poor electrical contact (poor interfacial bonding), but that photo-deposition of the Cu precursor directly on the ZnO surface improves interfacial bonding (the atom-by-atom method to build pn-heterostructure). In contrast, performing photo-deposition on a post-heated ZnO surface, where midgap states to some extents have been healed, significantly improves the phenol photodegradation performance (48.3 % degradation).

Previous work has also shown beneficial photo-degradation activity of CuO/ZnO and $\text{Cu}_2\text{O}/ZnO$ heterostructures, although these works have not quantified the influence of interfacial properties. Wang et al.⁴⁵ prepared ZnO whiskers decorated with CuO particles by a photo-deposition method. They observed much improved photocatalytic decomposition of methyl orange from the photo of the composite compared to physical mixtures of ZnO and CuO. However, they reported that too high deposition of CuO decreased the photocatalytic activity. Mahrsi and workers prepared $\text{Cu}_2\text{O}/\text{CuO}@ZnO$ composites by photo-deposition of $\text{Cu}(\text{NO}_3)_2$ over ZnO nanorods.⁴⁶ The composites were found to be more effective in the photocatalytic decomposition of Rhodamine B and Remazol Brilliant Blue R

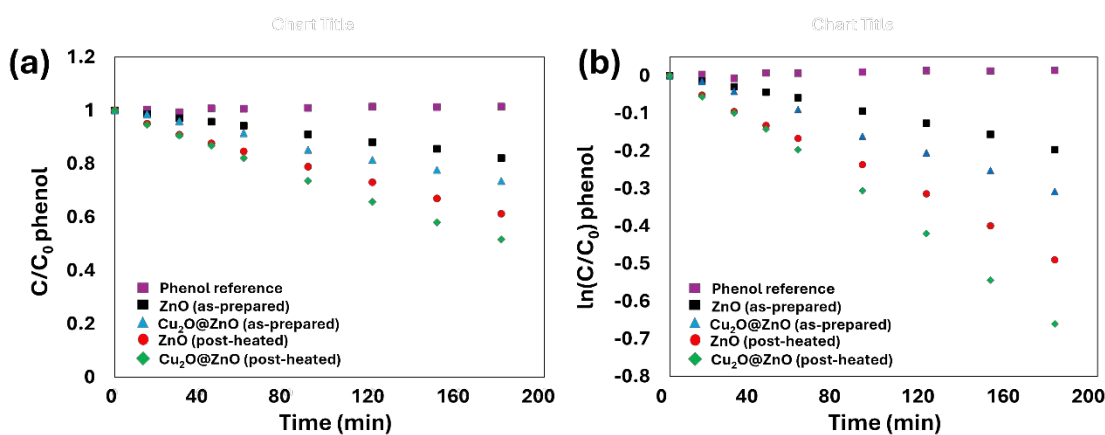


Fig. 8 (a) Normalized phenol concentration as a function of UVA illumination (365 nm). (b) Pseudo first-order plot for phenol removal. The initial phenol concentration was 60 ppm and the photocatalyst concentration was 1 g/L in all experiments. The control experiment with no photocatalyst is denoted “Phenol reference”.



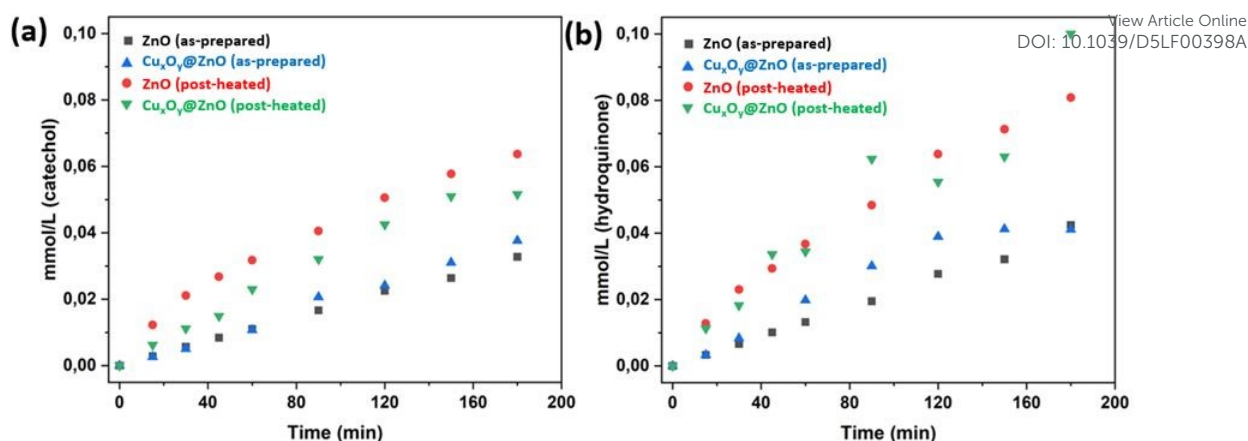
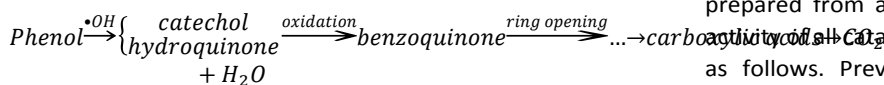


Fig. 9 (a) Formation of catechol during the decomposition of phenol. (b) Formation of hydroquinone during the decomposition of phenol.

compared to only ZnO rods. They also noticed that increasing copper loading decreased the photocatalytic activity.

The formation of the intermediate compounds catechol and hydroquinone was clearly observed (Fig. 9a, b). No other intermediates were detected under our experimental conditions. These species are primary degradation products of phenol resulting from attack by OH and O₂ radicals, which abstract delocalized π -electrons from the aromatic ring, and initiates ring opening and subsequent formation of carboxylates (acetate and formate; RCOO), whose anions can bind to the catalyst, as follows:⁴⁷



At start (0 min), neither catechol nor hydroquinone were detected. However, as the UV-illumination proceeded, both intermediates started to form. The formation of intermediates was highest for post-heated ZnO and Cu₂O@ZnO catalysts. The photodegradation rate of phenol was also higher on post-heated ZnO-based samples, 1.5 times higher for post-heated ZnO and 1.4 times for post-heated Cu₂O@ZnO.

It is well-established that photo-deposition products tend to localize at regions where photogenerated electrons or holes accumulate, such as specific crystal facets or surface defects like oxygen vacancies. Therefore, an additional consideration is the

influence of surface state, defect density, and crystallinity on the photo-deposition process. While defective surfaces generally are reported to enhance photocatalytic activity on ZnO,³⁹ they may be less favourable for photo-deposition functionalization since they act as traps for excitons.⁴⁸

Comparing the phenol photo-degradation rate for post-heated ZnO and Cu₂O@ZnO-post-heated catalysts, we see that the normalized rate is only slightly higher for the Cu₂O@ZnO p-n type heterostructure catalysts, while it is significantly higher than the corresponding Cu₂O@ZnO prepared from as-prepared ZnO nanorods (by a factor of almost 3). The Cu₂O@ZnO catalyst prepared from as-prepared ZnO nanorods shows the lowest activity of all catalysts studied. These results can be rationalized as follows. Previous photocatalytic photo-oxidation studies have shown that surface defects and hydroxyls play an important role in nanostructured ZnO photocatalysts.⁴⁹ Loss of reactive hydroxyls during heating of ZnO lead to reduced activity (which is e.g. evident in the loss of Zn-OH deduced from the O1s spectra in XPS).^{39, 50} The data shown in Fig. 6 shows that the deep level emission band in ZnO quenched upon post-heating which we attribute to removal of active OH and hydride species at defective ZnO lattice sites. This conclusion apparently contradicts the observation that the phenol degradation rate is about 1.5 times higher after post-heating ZnO. However, the detrimental effect of synthesis impurity site-blocking dominates

Table 1 Summary of the photocatalytic studies. Rate constants for phenol degradation and the formation of the catechol and hydroquinone intermediates, normalized for surface area, are reported.

Sample	Phenol decomposition rate (min ⁻¹)	Phenol decomposition rate ($\mu\text{mole min}^{-1} \text{m}^{-2}$)	Catechol formation rate ($\mu\text{mole min}^{-1} \text{m}^{-2}$)	Hydroquinone formation rate ($\mu\text{mole min}^{-1} \text{m}^{-2}$)	Specific surface area (g/m ²)
ZnO as-prepared	0.0011	0.094	0.03	0.03	7.1±0.2
ZnO post-heated	0.0017	0.22	0.05	0.07	6.1±0.2
Cu ₂ O@ZnO as-prepared	0.0026	0.086	0.02	0.02	11.7±0.2
Cu ₂ O@ZnO post-heated	0.0037	0.23	0.04	0.06	7.8±0.4



the reactivity on the as-prepared ZnO, as we previously have reported on ZnO synthesised by the same methods.³⁹

It is observed that the first hydroxylation step is larger on the post-heated ZnO than the post-heated Cu₂O@ZnO, which qualitatively support that defective ZnO sites (primarily O vacancies) are responsible for the high activity on the former photocatalyst due larger abundance of those (since Cu₂O blocks some of these sites).

These sites are gradually consumed and are not catalytic. In contrast, the reaction rate for subsequent steps is faster on the post-heated Cu₂O@ZnO, which we argue is due to the catalytic generation of radicals at the Cu₂O/ZnO interface where interfacial charge transfer is enhanced (as inferred from Fig. 6). Hence, the mechanism for photodecomposition is different on the ZnO and Cu₂O@ZnO photocatalysts and they expose different active sites for phenol photodecomposition: reactive hydroxyls on ZnO and enhanced radical generation on the post-heated Cu₂O@ZnO. The observed differences between the two Cu₂O@ZnO catalysts can be explained by their different interfacial structure and a more developed electronic interaction between Cu₂O and ZnO in the samples prepared using post-heated ZnO. These features are consistent with enhanced electron–hole pair separation in the latter, which correlates with improved performance of the resulting pn-heterojunction photocatalyst.

4. Conclusions

In this work we have presented a simple wet chemical method to prepare Cu₂O@ZnO oxide pn-type heterostructure catalysts by employing photo-deposition of a [Cu(EDTA)]²⁻ complex over ZnO sea urchin-like structures. This method yielded simultaneous deposition of Cu homogeneously distributed over the ZnO structures with possible excess Cu forming larger clusters at the tips of the ZnO nanorods. The Cu₂O@ZnO pn-heterojunction prepared on pre-heated ZnO showed higher efficiency (1.4 times) for photodegradation of phenol compared to the catalyst prepared on as-prepared ZnO, degrading 48.3 % of the phenol after 180 minutes UV-illumination. The ZnO post-heating step results in ZnO with well-developed facets and reduced amount of organic surface contaminants leading to a better contact between the ZnO and Cu₂O phases, which may improve electron-hole separation of photo-excited electron-hole pairs across their interfaces. Our work highlights the importance of employing well-crystallized materials with minimal surface impurities to achieve good interfacial bonding to improve interfacial charge transfer when preparing pn-type heterostructure catalysts by wet chemical methods.

Author contributions

FGS – Formal analysis, Investigation, Methodology, Validation, Visualization, Writing – original draft, review & editing; ED - Formal analysis, Investigation; YY - Formal analysis, Investigation, Writing – review & editing; SK – Investigation, Writing – review & editing; JH - Writing – Formal analysis,

review & editing; JT – Investigation, Formal analysis; ED – Investigation, Writing – review & editing; Supervision, Writing – review & editing; Writing – Supervision, review & editing; BIS – Methodology, Writing – review & editing; LÖ – Conceptualization, Formal analysis, Funding acquisition, Methodology, Project administration, Resources, Supervision, Validation, Visualization, Writing – original draft, review & editing.

Conflicts of interest

There are no conflicts to declare.

Data availability

Additional data is available as Supplementary Information.

Acknowledgements

The authors would like to thank the European Commission Horizon under the 2020 Framework Programme and the Swedish Research Agency Formas for the funding (grant no 2020-03196), in the frame of the collaborative international consortium GreenWaterTech, financed under the ERA-NET AquaticPollutants Joint Transnational Call (869178-AquaticPollutants). This ERA-NET is an integral part of the activities developed by the Water, Oceans, and AMR Joint Programming Initiatives. B.I.S. is grateful to BNSF project KP-06-N-59/11.

Notes and references

1. R. Suresh, L. Gnanasekaran, S. Rajendran, M. Soto-Moscoso, W. H. Chen, P. L. Show and K. S. Khoo, *Environ Sci Technol*, 2023, **31**, 103149.
2. A. S. Morshedy, E. M. El-Fawal, T. Zaki, A. A. El-Zahhar, M. M. Alghamdi and A. M. A. El Naggar, *Inorg Chem Commun*, 2024, **163**, 112307.
3. H. Al-Mohamadi, S. A. Awad, A. K. Sharma, N. Fayzullaev, A. Tavarra-Aponte, L. Chiguala-Contreras, A. Amari, B. Rodrigues, C., M. A. Tahoona and H. Esmaeili, *Catalysts*, 2024, **14**, 420.
4. S. Madronich, in *Environmental UV Photobiology*, eds. A. R. Young, J. Moan, L. O. Björn and W. Nultsch, Springer, New York, 1993.
5. W. Y. Teoh, J. A. Scott and R. Amal, *J Phys Chem Lett*, 2012, **3**, 629–639.
6. R. Mishra, S. Bera, R. Chatterjee, S. Banerjee, S. Bhattacharya, A. Biwas, S. Mallick and S. Roy, *Appl Surf Sci Adv*, 2022, **9**, 100241.
7. S. Das and V. C. Srivastava, *Nanotechnology Reviews*, 2018, **7**, 267–282.
8. J. X. Liu, H. Wang, H. Wu, Y. Yang, C. Wang, Q. Wang, B. Jia and J. Zheng, *J Mater Chem A*, 2024, **12**, 20838.
9. S. Sun, *Nanoscale*, 2015, **7**, 10850.
10. R. Marschall, *Adv Funct Mater*, 2014, **24**, 2421–2440.
11. K. Luo, W. Hu, J. Wei, Q. Zhang, Z. Wu, D. Li, F. Miao, Y. Huang, M. Xu, J. Ma, C. Li, G. Chen, R. Han, X. L. Wang, X.



- Cui and P. Ruterana, *Phys Chem Chem Phys*, 2021, **23**, 10768.
12. Y. Wang, S. Li, H. Shi and K. Yu, *Nanoscale*, 2012, **4**, 7817.
13. L. Zhu, H. Li, Z. Liu, Y. Xie and D. Xiong, *The Journal of Physical Chemistry C*, 2018, **122**, 9531–9539.
14. A. Dastider, H. Saha, M. J. F. Anik, M. Jamal and M. M. Billah, *RCS Advances*, 2024, **14**, 11677–11693.
15. U. Özgür, Y. I. Alivov, C. Liu, A. Teke, M. A. Reshchikov, S. Dogan, V. Avrutin, S. J. Cho and H. Morkoc, *J Appl Phys*, 2005, **98**, 041301.
16. S. B. Zhang, S. H. Wei and A. Zunger, *Physical Review B*, 2001, **63**, 075205.
17. Y. Liu, C. Chen, J. Valdez, D. M. Meira, W. He, Y. Wang, C. Harnagea, Q. Lu, T. Guner, H. Wang, C. H. Liu, Q. Zhang, S. Huang, A. Yurtsever, M. Chaker and D. Ma, *Nat Commun*, 2021, **12**, 1231.
18. R. Saravanan, S. Karthikayan, V. K. Gupta, G. Sekaran, V. Narayanan and A. Stephen, *Materials Science and Engineering: C*, 2013, **33**, 91–98.
19. B. Li and Y. Wang, *Superlattices and Microstructures* 2010, **47**, 615–623.
20. B. Abebe, D. Tsegaye, C. Sori, R. C. K. R. Prasad and H. C. A. Murthy, *ACS Omega*, 2023, **8**, 9597–9606.
21. A. Muzakki, H. Shabrany and R. Saleh, *THE 3RD INTERNATIONAL CONFERENCE ON ADVANCED MATERIALS SCIENCE AND TECHNOLOGY (ICAMST)*, 2016, **1725**, 020051.
22. S. Kuld, M. Thorhauge, H. Falsig, C. F. Elkjaer, S. Helvig, I. Chorkendorff and J. Sehested, *Science*, 2016, **352**, 969–974.
23. A. Beck, M. A. Newton, M. Zabilskiy, P. Rzepka, M. G. Willinger and J. A. van Bokhoven, *Angew Chem Int Edit*, 2022, **61**, e202200301.
24. J. A. Montero, T. Welearegay, H. Stopfel, T. Dedova, I. O. Acik and L. Österlund, *RCS Advances*, 2021, **11**, 10224.
25. M. Okazaki, Y. A. Wang, T. Yokoi and K. Maeda, *J Phys Chem C*, 2019, **123**, 10429–10434.
26. T. Butburee, K. Papasara, P. Hirunsit, Z. Sun, Q. Tang, P. Khemthong, W. Sangkhun, W. Thongsuwan, P. Kumnorkeaw, H. Wang and K. Faungnawakij, *J Mater Chem A*, 2019, **7**, 8156.
27. L. Clarizia, G. Vitiello, R. B. Vadell, J. Sa, R. Marotta, I. D. Somma, R. Andreozzi and G. Luciani, *International Journal of Molecular Sciences*, 2023, **24**, 2004.
28. G. Wu, N. Guan and L. Li, *Catal Sci Technol*, 2011, **1**, 601–608.
29. S. S. Djokic and L. Magagnin, *Metallization of semiconductors and nonconductive surfaces from aqueous solutions*, Springer, New York, 2014.
30. T. Baran, A. Visivile, M. Busch, X. He, S. Wojtyla, S. Rondinini, A. Minguzzi and A. Vertova, *Molecules*, 2021, **26**, 7271.
31. P. Venev, B. I. Stefanov, V. Milusheva, B. Tzaneva and V. Videkov, *Proc. 12th National Conference with International Participation "Electronica 2021"*, 2021.
32. B. I. Stefanov, V. Milusheva, H. G. Kolev and B. Tzaneva, *Catal Sci Technol*, 2022, **13**, 7027.
33. M. A. Sliem, T. Hikov, Z. A. Li, M. Spasova, M. Farle, D. A. Schmidt, M. Havenith-Newen and R. A. Fischer, *Phys Chem Chem Phys*, 2010, **12**, 9858–9866.
34. Y. Chen, H. Zhao, B. Liu and H. Yang, *Applied Catalysis B: Environmental*, 2015, **163**, 189–197.
- G. Menagen, J. E. Macdonald, Y. Shemesh, I. Popov and U. Banin, *J Am Chem Soc*, 2009, **131**, 17406–17411.
36. M. Law, L. E. Greene, J. C. Johnson, R. Saykally and P. Yang, *Nature Materials*, 2005, **4**, 455–459.
37. N. S. McIntyre and M. G. Cook, *Analytical Chemistry*, 1975, **47**, 2208–2213.
38. E. H. Park, J. Jung and H. H. Chung, *Chemosphere*, 2006, **64**, 432–436.
39. F. G. Svensson, E. Djurberg, S. Kim, G. Westin and L. Österlund, *Langmuir*, 2025, **41**, 28399–28410.
40. A. Kwiatkowski, J. Smulko, K. Drozdowska, L. Österlund and T. Welearegay, *Sol Energ Mat Sol C*, 2024, **273**, 112940.
41. T. J. Frankcombe and Y. Liu, *Chem Mater*, 2023, **35**, 5468–5474.
42. M. Soltanmohammadi, E. Spurio, A. Gloystein, P. Luches and N. Nilius, *Physica Status Solidi A*, 2023, **220**, 2200887.
43. N. Kumar, S. S. Parui, S. Limbu, D. K. Mahato, N. Tiwari and C. R.N., *Materials Today: Proceedings*, 2021, **41**, 237–241.
44. J. Thyr, J. Montero, L. Österlund and T. Edvinsson, *ACS Nanoscience Au*, 2021, **2**, 128–139.
45. J. Wang, X. M. Fan, D. Z. Wu, J. Dai, H. Liu, H. R. Liu and Z. W. Zhou, *Appl Surf Sci*, 2011, **258**, 1797–1805.
46. M. I. Mahrsi, B. Chouchene, T. Gries, V. Carre, G. Medjahdi, F. Ayari, L. Balan and R. Schneider, *Journal of Environmental Chemical Engineering*, 2024, **12**, 113072.
47. A. Turki, C. Guillard, F. Dappozze, Z. Ksibi, G. Berhault and H. Kochkar, *Appl Catal B-Environ*, 2015, **163**, 404–414.
48. J. Fang, H. Fan, Y. Ma, Z. Wang and Q. Chang, *Appl Surf Sci*, 2015, **332**, 47–54.
49. N. M. Flores, U. Pal, R. Galeazzi and A. Sandoval, *Rsc Adv*, 2014, **4**, 41099.
50. D. A. Giannakoudakis, J. A. Arcibar-Orozco and T. J. Bandoz, *Applied Catalysis B: Environmental*, 2015, **174**, 96–104.



Data availability statements

Photo-deposition of Cu₂O on Pre-Annealed ZnO Nanorods Yields pn-Type Heterostructures with Enhanced Photocatalytic Activity

*Fredric G. Svensson, Erik Djurberg, Yige Yan, Seohan Kim, Jiri Henych, Jakub Tolasz, Frederic Dappozze, Stephane Parola, Chantal Guillard, Bozhidar I. Stefanov, and Lars Österlund**

The data supporting this article have been included as part of the Supplementary Information. Supplementary information. See DOI: [URL – format <https://doi.org/DOI/xxx>]

